FerroTag: A Paper-based mmWave-Scannable Tagging Infrastructure

Zhengxiong Li[1], Baicheng Chen[1], Zhuolin Yang[1], Huining Li[1],
Chenhan Xu[1], Xingyu Chen[1], Kun Wang[2], Wenyao Xu[1]
[1] University at Buffalo, the State University of New York, Buffalo, New York, USA
[2] University of California, Los Angeles, Los Angeles, California, USA

ABSTRACT

Inventory management is pivotal in the supply chain to supervise the non-capitalized products and stock items. Item counting, indexing and identification are the major jobs of inventory management. Currently, the most adopted inventory technologies in product counting/identification are using either the laser-scannable barcode or the radio-frequency identification (RFID). However, the laser-scannable barcode is entangled by an alignment issue (i.e., the laser reader must align with one barcode in line-of-sight), and the RFID is economically and environmentally unfriendly (i.e., high-cost and not naturally disposable). To this end, we propose FerroTag which is a paper-based mmWave-scannable tagging infrastructure for the next generation inventory management system, featuring ultra-low cost, environment-friendly, battery-free and in-situ (i.e., multiple tags can be simultaneously processed outside the line-of-sight). FerroTag is developed on top of the *FerroRF* effects. Specifically, the magnetic nanoparticles within the ferrofluidic ink reply to probing mmWave with classifiable features (i.e., the *FerroRF* response). By designating the ink pattern and hence the location of particles, the related *FerroRF* response can be modified. Thus, a specifically designated ferrofluidic ink printed pattern, which is associated with a unique *FerroRF* response, is a remotely retrievable (a.k.a., mmWave-scannable) identity. Furthermore, we augment FerroTag by designing a high capacity pattern system and a fine-grained identification protocol such that the capacity and robustness of FerroTag can be systematically improved in mass product management in inventory. Last but not least, we evaluate the performance of FerroTag with 201 different tag design patterns. Results show that FerroTag can identify tags with an accuracy of more than 99% in a controlled lab setup. Moreover, we examine the reliability, robustness and performance of FerroTag under various real-world circumstances, where FerroTag maintains the accuracy over 97%. Therefore, FerroTag is a promising tagging infrastructure for the applications in inventory management systems.

CCS CONCEPTS

• **Computer systems organization**;

Corresponding E-email: wenyaoxu@buffalo.edu (W.X.); wangk@ucla.edu (K.W.).

SenSys '19, November 10–13, 2019, New York, NY, USA

ACM ISBN 978-1-4503-6950-3/19/11…$15.00
https://doi.org/10.1145/3356250.3360019

ACM Reference Format:
Zhengxiong Li[1], Baicheng Chen[1], Zhuolin Yang[1], Huining Li[1], and Chenhan Xu[1], Xingyu Chen[1], Kun Wang[2], Wenyao Xu[1]. 2019. *FerroTag*: A Paper-based mmWave-Scannable Tagging Infrastructure . In *The 17th ACM Conference on Embedded Networked Sensor Systems (SenSys '19), November 10–13, 2019, New York, NY, USA.* ACM, New York, NY, USA, 14 pages. https://doi.org/10.1145/3356250.3360019

1 INTRODUCTION

An impressive amount of capital in the U.S., about 1.1 trillion dollars in cash which are equivalent to 7% of the entire U.S. GDP, is tightly associated with inventories [13]. As a result, inventory management (i.e., the supervisory mechanism for tracking the flow of goods from manufacturers to warehouses and from storage to the point of sale [2]) has become a critical component in the whole commercialized business. According to the newest 2019 report from Statista [15], business respondents, who are all manufacturers and retailers, rated the warehouse management as the most important business investment in 2017 as 90% of the inventory are stationary (e.g., stored in warehouses) [14]. The reports also indicate that most of companies are willing to upgrade the current existing inventory management systems to further promote efficiency in daily routines and manage business growth [4].

Currently, there are two types of tagging technologies employed in most of existing inventory management systems, i.e., barcode and radio-frequency identification (RFID) [1]. Barcode is a printed patternized identity which is read by a laser scanner [7]. However, since barcode technology relies on invisible/visible light (i.e., a medium can hardly travel through obstacles) for information acquisition, the scanner must align with the barcode in line-of-sight to recognize the identity [65]. In addition, ordinal scanners limit to processing one barcode at a time [21]. Different from the printable barcode, an RFID is an electronics consisting of a circuit and an antenna, which encodes and transmits the data/identity in RF wave (i.e., a medium can pass through barriers) [26]. Although RFID has the advantage over the barcode in term of scanning efficiency, there is a significant hindrance causing the financial and the environmental costs. One RFID tag costs from $0.18 - 30$ US dollars [3, 16]. Moreover, RFID tags cannot be naturally degraded after the use and become a kind of e-waste in most of cases [55]. Giving the fact that the inventory system is essential for business growth, there is an urgent need to develop a better paradigm for tagging technologies.

To this end, we introduce FerroTag as an advanced tagging infrastructure to promote inventory management system, i.e., a critical part in the modern commercialized business. In particular, FerroTag is featured as **(1) Ultra-low cost:** the tag is highly affordable for large scale deployment; **(2) Environment-friendly:** the tag is based on ordinal papers and with non-toxic inks, which are safely

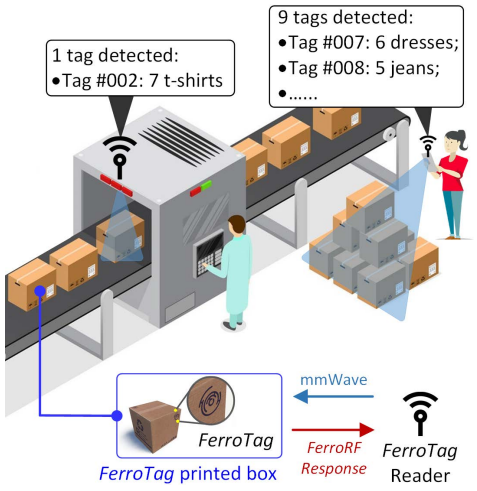

Figure 1: FerroTag, a paper-based mmWave-scannable tagging infrastructure, can replace the traditional tagging technologies for mass product counting and identification in inventory management.

disposable and naturally degradable; **(3) Battery-free:** the tag is completely passive requiring no power supply; **(4) In-situ:** multiple tags are accurately read by a scanner outside the line-of-sight. As shown in Figure 1, the application scenes of FerroTag include manufacturing factories, warehouses and retail offices.

Specifically, FerroTag is a paper-based mmWave-scannable tagging infrastructure. A pattern printed by naturally degradable ink is served as an identity [61]. Thus, it is highly economical, environmentally harmless and fully passive in its origin. In order to realize FerroTag, we need to address two technical challenges in this work: *(a) design and implement a paper-based mmWave-scannable tagging infrastructure for the inventory management system.* The foundation of FerroTag rests on the *FerroRF* effects. When RF signals meet surfaces and objects, a responsive RF signal will be generated [78]. In our application, when there is an RF signal passing through, a ferrofluidic ink print will generate a recognizable response (hereafter, the *FerroRF* response) which is associated with the ferrofluidic print pattern (i.e., the tag identity). To retrieve and recognize the identity, a fine-grained response analysis protocol is developed. First of all, to protect the *FerroRF* response from distortions, a range resolution analysis and an envelope correlation function are applied. Secondly, we extract a set of critical scalar features (n = 25), including ten most impactful ones based on Mel-Frequency Cepstral Coefficients. At the end, the selected features are fed into a classifier containing a cluster of decision trees (m = 150) for identification. In addition, by analyzing the angle of arrival, multiple tags can be simultaneously detected and identified. *(b) Model and optimization of the FerroRF effects for high capacity.* We first investigate and establish a mathematical model of the *FerroRF* effects. The *FerroRF* response is generated by the magnetic nanoparticles within the ferrofluidic ink. Since the quantity and the arrangement (i.e., three-dimensional locations) of particles are varying along with any variation in a ferrofluidic ink printed pattern, a unique pattern can be served as a non-contact retrievable identity as it can generate a unique *FerroRF* response. Secondly, with the in-depth modeling and understanding of the *FerroRF* effects and response, we study a systematic approach to optimize the variation of the *FerroRF* effects by designate tag patterns such that it contains only succinct geometric features but can be used to room high-capacity identities in the tagging infrastructure. More specifically, we investigate and evaluate an innovative nested pattern for tagging design in FerroTag, which can provide a large number of identities with regulations to a vast amount of products in inventories.

Our contribution can be summarized in three-fold:

- We investigate the *FerroRF* effects and discover the magnetic nanoparticles within the ferrofluidic ink modulates probing mmWave with classifiable characteristics. Moreover, we model and advance the *FerroRF* infrastructure with an innovative nested tag pattern.
- We design and implement FerroTag with one working prototype machine. Specifically, we develop a new hardware and software stack support, and retrofit a commodity printer into the application of FerroTag fabrication. It is a paper-based mmWave-scannable tagging infrastructure. Each tag is made with low-cost, naturally degradable paper and ferrofluidic ink. Outside the line-of-sight, multiple tags can be remotely scanned by a cost-efficient mmWave probe to extract the identities.
- We evaluate FerroTag from three aspects. First, we study the spec of our infrastructure including cost, time budget, sensing accuracy and more. Second, we test the reliability with variances in sensing distances, orientations, environments, barriers and more. Finally, we investigate the performance of FerroTag and measure the stability in a case study on complex scenes.

2 BACKGROUND AND PRELIMINARIES

2.1 *FerroRF* Effects

Ferrofluidic ink is colloidal liquids, whose core components are magnetic nanoparticles (e.g., ferrite compound-Magnetite powder), carrier fluid that suspends the nanoparticles (e.g., organic solvent), and the surfactant that coats each magnetic nano-particles [77]. The quantity and the arrangement of these magnetic nanoparticles reflect into the unique characteristic frequency responses when tags are probed by broadband radio frequency (RF) signals as shown in Figure 2. When a fundamental tone is passed through the ferrofluidic ink, magnetic nanoparticles modulate the response signal and generate additional frequency tones besides the fundamental one as formulated in Section 2.2.

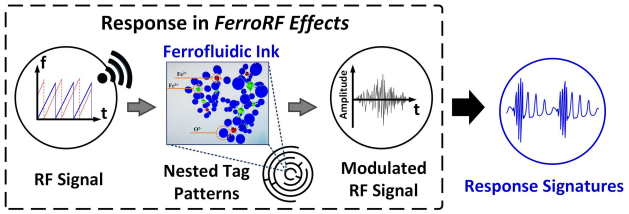

Figure 2: The ferrofluidic pattern generates a *FerroRF* response under the RF beam. The *FerroRF* response is associated with intrinsic physical characteristics of tag pattern.

mmWave is an emerging technology (e.g., 5G network) and it is worth to mention that object (e.g., tags) presence detection, tracking and localization through mmWave signals are intensively studied in the past years [19, 75, 81, 83, 85]. In contrast to other RF sensing modalities such as WiFi [79] and acoustics [48], mmWave has an excellent performance in term of the directionality and owns the superiority in high tolerance to ambient noises (e.g., sound, light, and temperature) and less surface scattering. Furthermore, mmWave facilitates a micron-level shape change resolution making it feasible to monitor the pattern shape change, which in case of shape size occurs at the range of 2-3mm [69]. Considering that mmWave is becoming the key carrier in the next-generation wireless communication, we will investigate the *FerroRF* effects under the applications of mmWave signals.

Hypothesis: It is indeed the *FerroRF* response (i.e., harmonics or inter-modulation) that contains the unique characteristics of the tag, which can be treated as an intrinsic and persistent identity of the tag. Different geometric shapes and sizes of ink patterns on tags can be meticulously designed; these discrepancies are sufficient to alter the frequency responses and induce unique, measurable fingerprints which associate with the ink patterns. *Therefore, it is possible to utilize a mmWave probe to force tags to radiate the response signature that reflects their unique properties and can be used for object counting and identification.*

2.2 Modeling on *FerroRF* Effects

In this part, we further explore the *FerroRF* effects. Before completely understanding the tag modulation on the response signal, it is crucial to model the *FerroRF* effects. When a fundamental tone is passed through the tags, the ferrofluidic patterns modulate the response signal and generate additional frequency tones besides the fundamental one as formulated in Equation (1):

$$r(f,\tau,t) = R_{f,t}(\tau) \bigotimes h_f(t), \tag{1}$$

where $r(f,\tau,t)$ is the signal modulation function of ferrofluidic due to the stimulation of millimeter wave [74]. $R_{f,t}(\tau)$ is the signal reflection function based on: τ-volume makeup of ferrofluidic, f-range of frequency, and t-time instant. $\bigotimes$ stands for convolution computing and h_f (t) is the ideal band-pass filter function for the carrier bandwidth [41]. In the following equations, we model the relation between τ-volume makeup of ferrofluidic and signal modulation function, in which the volume makeup, consisting of three dimensions, is the geometric pattern that can be manipulated with tag pattern design.

$$\begin{cases} R_{f,t}(\tau) = \dfrac{R_{f,t}(\tau)_1}{R_{f,t}(\tau)_2}, \\ R_{f,t}(\tau)_1 = exp(2\gamma_d(\tau)L)(\gamma_d(\tau)-\gamma_0(\tau))(\gamma(\tau)+ \\ \qquad \gamma_d(\tau)) + (\gamma_0(\tau)+\gamma_d(\tau))(\gamma(\tau)-\gamma_d(\tau)), \\ R_{f,t}(\tau)_2 = -exp(2\gamma_d(\tau)L)(\gamma_d(\tau)+\gamma(\tau))(\gamma_0(\tau)+ \\ \qquad \gamma_d(\tau)) + (\gamma_0(\tau)-\gamma_d(\tau))(\gamma(\tau)-\gamma_d(\tau)), \\ \gamma^2(\tau) = \dfrac{\pi^2}{a^2} - \omega^2\epsilon_0\mu_0\epsilon\mu^*(\tau), \end{cases} \tag{2}$$

$R_{f,t}(\tau)$ has two parts in the mathematical presentation. γ_0 and γ are the propagation constants in the empty and ferrofluidic parts of the wave-guide, respectively; γ_d is the propagation constant of the wave in the dielectric. L is the thickness of dielectric insertion. d represents the diameter of the ferromagnetic particles; a is the size of the wide wall of the wave-guide; π is the ratio of a circle's circumference to its diameter. ϵ_0 and μ_0 are the electric and magnetic constants, respectively; ϵ and μ^* are the permittivity and the permeability of the medium that fills the wave-guide cross section, in which ferrofluidic presents, respectively. This shows the relationship between ferrofluidic's permeability of millimeter wave and and the volume makeup, which we further model with Equation 3.

$$\begin{cases} \mu^* = 1 + \chi_m{}'(\tau) - j\chi_m{}''(\tau), \\ \chi_m{}'(\tau) = \dfrac{\gamma\tau ML(\sigma)}{\omega H_n} \dfrac{(1+\eta^2)^2 {H_n}^4 + (\eta^2-1){H_n}^2}{(1+\eta^2)^2 {H_n}^4 + 2(\eta^2-1){H_n}^2 + 1}, \\ \chi_m{}''(\tau) = \dfrac{\gamma\tau ML(\sigma)}{\omega H_n} \dfrac{\eta {H_n}^2(1+{H_n}^2(1+\eta^2))}{(1+\eta^2)^2 {H_n}^4 + 2(\eta^2-1){H_n}^2 + 1}, \end{cases} \tag{3}$$

where τ is the volume makeup of ferrofluid which is manipulated with our tag design, as shown in Figure 3. $\chi_m{}'$ and $\chi_m{}''$ are the real and imaginary parts of the magnetic susceptibility, respectively [74]. H_n is the reduced magnetic field $\eta = \xi(\frac{1}{L(\sigma)} - \frac{1}{\sigma})$; $H_n = \gamma\frac{H}{\omega}$; $\sigma = \frac{\mu_0 M_d V}{kT}H$, σ is a combined parameter of the magnetic fluid; M_d is a saturation magnetization of the solid magnetic. $V = \frac{\pi d^3}{6}$ is the volume of a ferromagnetic particle; ξ is the damping constant of the electromagnetic wave in the magnetic fluid; For spherical ferromagnetic particles, it is assumed that the dielectric properties of the magnetic fluid are independent of the magnetic field [73, 74]. To summarize the foregoing exploration, *the FerroRF response can be affected by adjusting the ferrofluidic ink pattern shape and size.*

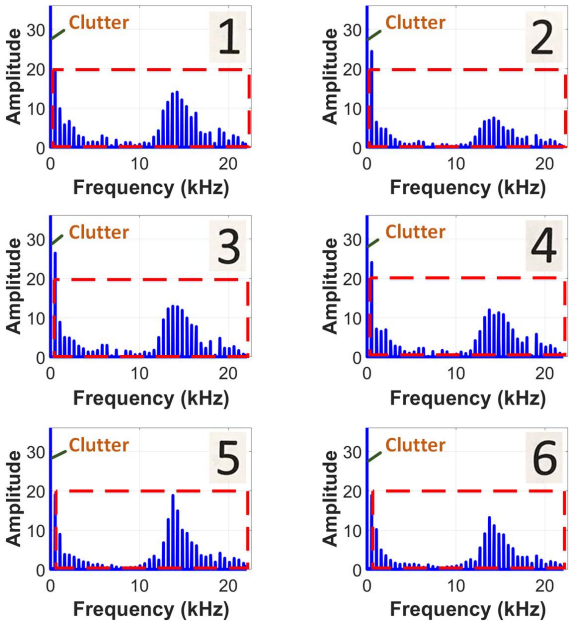

Figure 3: The *FerroRF* responses (in the red box) of six different patterns (in the upper right corner) are distinct in both frequency spectrum and amplitude after the modulation, indicating the feasibility of FerroTag counting and identification.

2.3 The *FerroRF* Effects on Tags

Proof-of-concept: To gain evidence on the validation of the *Hypothesis*, we conducted a preliminary experiment using 6 different tags with different patterns. Each tag pattern is attached to the right in Figure 3. These tag patterns are made by ferrofluidic ink with a regular copy paper following the Arabic numerals shapes of 1 to 6, which are different from aspects of the size and the shape. Six different tags are stimulated with the mmWave probe with a distance from the devices. The reflected signal profile is explored in the spectrum domain. As shown in the range frequency spectrum graph (see Figure 3), the x-axis is the frequency, and the y-axis is the amplitude of the received signal. The various sub-carrier frequencies can be clearly observed that, separated from the clutter of the artifacts, their *FerroRF* responses are distinct at the frequency and amplitude. To conclude, the results are significantly promising, implying that given the massive amount of tags, variations have sufficient space to be served as powerful identity resources.

A Study on Package Box: After we confirm the *FerroRF* responses from different tag patterns are diverse, there is still one remaining challenge. In real-world applications, FerroTag can be placed on the package box. As a result, we need to investigate whether the surroundings, such as package box, will disturb the *FerroRF* response and interfere the tag identification. We investigate an example of the interference from the package box, when a mmWave signal comes through the tag, in Figure 4. We first put a package box without the tag before the mmWave probe. As shown in the range frequency spectrum graph (see Figure 4(a)), where the x-axis is the frequency of the received signal, the y-axis is the power spectral density (PSD) [82] of the received signal, we can observe that the reflective signal from the package box is stable and visible. Furthermore, we attach a tag on the package box, and then reacquire and analyze the mmWave signal as shown in Figure 4(b). A comparison between these two trial results confirms that these two PSDs are significantly distinguishable, which proves the feasibility of the tagging infrastructure in real practice.

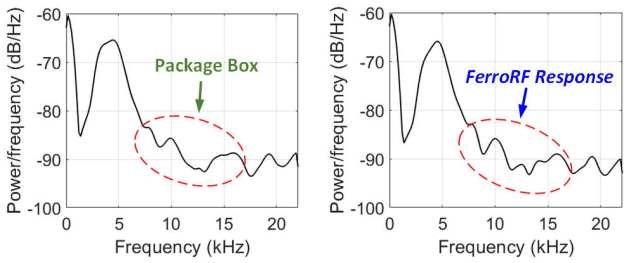

(a) The object package PSD analysis without the tag.

(b) The object package PSD analysis with the tag.

Figure 4: An example of the object package PSD estimation analysis without and with interference from FerroTag.

3 FERROTAG SYSTEM OVERVIEW

We introduce FerroTag, a paper-based mmWave-scannable tagging infrastructure to facilitate mass object counting/identification of the inventory management. The end-to-end system overview is shown in Figure 5.

Tag Fabrication: The primary physical components of FerroTag are a series of ferrofluid patterns printed on a normal substrate, e.g., copy paper. The tag patterns can be highly customized. The tag can be manufactured via a variety of mass-produced, easy-to-use and widely accessible manufacturing methods.

Tag Scanning and Identification: A mmWave probe is proposed to remotely and robustly acquire the tag's *FerroRF* response for identification. Specifically, the probe transmits a mmWave signal and processes/demodulates the reflected response signal. Once receiving the data, the tag identification module first performs the preprocessing to correct the distortion and extracts the spatial-temporal features. After that, an effective classification algorithm is developed to count the tag number and recognize the tag identity.

4 TAG DESIGN AND IMPLEMENTATION

4.1 Basic Tag Pattern Study

To diffuse ferrofluidic materials in to the substrate, we print a ferrofluidic ink pattern directly on the substrate surface. In this process, the depth variation compared to its length and width is negligible (typically less than 0.1% on a tag that is 20x20mm), and the pattern can be considered pseudo-2D. As a result, we utilize 2D geometric shapes to characterize these ferrofluid printed pseudo-2D patterns and test the *FerroRF* response.

For designing an appropriate tag pattern, we analyze the area to perimeter ratios of some typical geometric shapes. The area to perimeter ratios of triangle, rectangle/square, pentagon, and circle are around $0.14l$, $0.25l$, $0.2l$, and $0.25l$, respectively. It is worth to mention that other shapes (e.g., hexagon, octagon, and decagon) can be decomposed by two or more regular shapes. Among our design in Figure 6, both the square and the circle have the highest area to perimeter ratio, but the circle saves more than 21% space compared to the square. Also, we notice while the tag pattern is more complex, the pattern has more forms of presentation (i.e. more potential component combinations and identity capacity under certain layouts). We further introduce a formal approach to generating a nested geometric for robust and high-capacity tag design.

4.2 Prototyping of FerroTag

4.2.1 FerroTag Pattern Design Systemization. In order to better characterize the tag capacity, we propose the *pattern complexity score* $\phi(z)$ of a tag pattern to evaluate the pattern complexity. Specifically, $\phi(z)$ is estimated in Equation (4):

$$\begin{cases} \psi = \sum_{0}^{L-1} z_i p(z_i), \\ \phi(z) = \sum_{0}^{L-1} (z_i - \psi)^2 p(z_i), \end{cases} \tag{4}$$

where z is the grayscale of the image, $p(\cdot)$ is the histogram of the image, L is the grayscale level, ψ is the average of z, and $\phi(z)$ represents the complexity of the tag, which is also the variance of the histogram [62]. As shown in Figure 7, all scores of the basic patterns ((a)-(h)) are below 200. Besides, the complexity of a nested pattern (see Section 5) is at least twice than that of the basic pattern. Therefore, we define the threshold as 400 empirically. When the score is larger than 400, the tag is treated as a nested one. Based on $\phi(z)$, the tag can then be categorized according to the corresponding rules in Section 4.1 and 5.

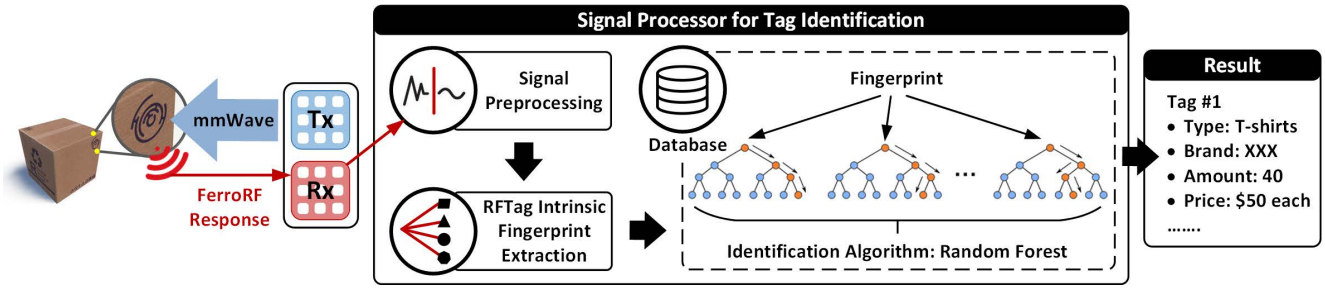

Figure 5: The system overview for FerroTag to in-situ identify the tag patterns. It comprises of the ultra-low cost tag with one mmWave sensing module in the front-end and one tag identification module in the back-end.

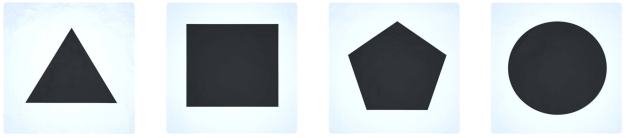

Figure 6: The design of four basic tag patterns.

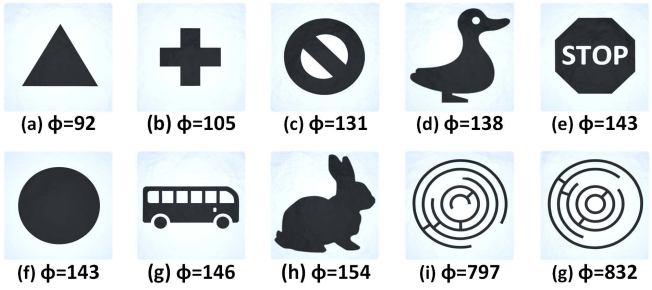

Figure 7: Representative tag designs with different complexity scores.

4.2.2 FerroTag Printing.

FerroTag Substrate: A paper based ferrofluidic ink printed tag is selected to achieve ultra-low cost, wireless, and secure counting of target objects. Papers are extremely low cost nowadays, and its price can become minimal in mass production [6].

FerroTag Printing Machine: To rapidly prototype the tags, we design a new FerroTag printing machine that is capable of producing printed tags. The prototype is based on a commodity printer, including two system support components.

Hardware Development: For the ease of implementation, we employ the modal of inkjet printers as the base of our printing machine. The main task is to revitalize an ink cartridge for ferrofludic printing. As shown in Figure 8(a), in order to replace printer ink or refill with ferrofluidic ink, a syringe is used to transfer ferrofluidic ink from container to cartridge safely. Syringe with needle diameter greater than 3*mm* is preferred due to the sealing nature of ferrofluidic ink, which causes plunge from pushing it into a cartridge. The needle needs to be kept at least 1*cm* below the surface of container and cartridge, as the ferrofluidic ink tends to form bubbles and splash over working area. In case that a cartridge is not revitalizable, we fabracate a 3D printable *Cartridge* that is physically compatible with manufacture's cartridge. After 3D printing the *Cartridge*, we inject the ferrofluidic ink without the need to remove ink residue, which is time-efficient and prevents the residue from contaminating ferrofluid. After injecting the ferrofluidic ink to the *Cartridge* and replacing manufacture cartridge with 3D printed *Cartridge*, procedures including print-head alignment, cleaning, and testing are carried out to remove ink residue in the printer. To prevent the printer from printing with an empty *Cartridge*, we design the ***Supply Manager*** module that estimates the ferrofluidic ink level in the printer based on *Cartridge*'s usage.

Software Development: To reduce the tag edit time, we develop a *FerroTag Generator* in the software stack that can efficiently generate tags in a mass scale, as shown in Figure 8(b). Users first input the number of tags to be printed, then the ***FerroTag Generator*** activates the *Randomizer* to generate parameters for the *Executor*. Afterwards, the *Executor* utilizes the parameters and follows Algorithm 1 (mentioned in Section 5) to generate tag image files.

After obtaining the generated patterns, we need a layout management to efficiently arrange tags on the substrate. Therefore, we add a custom-built *Layout manager* that transforms a set of tag images into a print-friendly printing layout, which is compatible with native printer drivers. The *Layout editor* first trims the tag images by removing white or transparent pixels, then, the size of each image is adjusted to user defined value from the *Size controller* via image processing technique such as bi-linear interpolation [47]. After that, the *Layout editor* concatenates images in a layout that best fits the paper size selected by users.

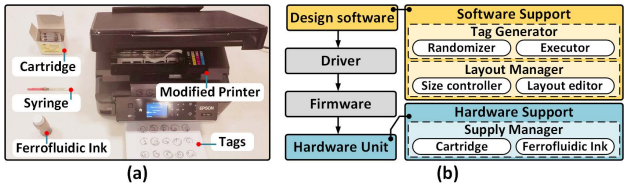

Figure 8: (a) shows the experimental setup for the retrofitted off-the-shelf printer employed for the mass manufacture. (b) illustrates the improved system architecture with hardware and software developments.

Alternative Fabrication Solution: With consumer-grade 3D printers becoming more pervasive, accessible, and reliable, users employ 3D printing technology to print FerroTag molds. As shown in Figure 9, we propose a new method of producing FerroTag utilizing the inexpensive, reusable, and durable 3D printed molds with basic geometric shape, as an alternative of modified inkjet printing. After the 3D printing stage, a firm tag can be drawn on the paper with a basic brush in seconds.

Figure 9: Several molds by 3D printing for the accessible manufacture.

Cost Analysis: The total printing costs originate from the printer and the consumable items. The commercial printer costs around $60 [12]. In our system, the 3D printing mold costs less than $1, the ferrofluidic ink costs around $9 for 60ml (around 0.15$/mL) [8], and the Staples copy paper we use costs $57 per 5000 sheets [9]. We find that per 10ml of ferrofluidic ink could produce more than 500 sheets and one sheet can carry more than 24 tag patterns. Therefore, the cost of one tag (i.e., ferrofluidic ink and paper) is less than *one cent*. Moreover, the cost can be further reduced under massive production.

5 FERROTAG ADVANCEMENT

In this section, we further investigate the advanced pattern design to enlarge the tag capacity and strengthen the robustness. The traditional approach is to utilize the stripe pattern design [28], which has a fixed stripe layout and completes the tag pattern change through the line width. However, such design is not applicable for this application since the ink can expand and involve the adjacent lines, which can severely devastate the corresponding *FerroRF* response. Therefore, we develop an advanced nested geometric design. Inspired by the concentric zone model [5], the nested pattern is a multiple-layer pattern produced through a series of iterations of components. With this multiple-layer iteration mode, the nested pattern allows tag capacity to increase exponentially with respect to the increment in number of layers, which shows a huge capacity for this application. Besides, we introduce a component, Hollow, between layers to aid resisting the ink expansion interference. Furthermore, learned from our preliminary design exploration from the volume of ferrofluidic ink, the design complexity as shown in Figure 3 and Figure 7, respectively, we propose the design protocol, containing three key components: spiral line, hollow, connection as shown in Figure 10.

Figure 10: The illustration of the advanced tag pattern design, including three components: hollow, connection and spiral line.

Spiral Line: FerroTag is based on a set of nested circles that effectively utilizes two dimensional substrate surface space. To reduce ferrofluid usage on paper substrate, we apply a set of nested arcs (*i.e.,* spiral lines) to substitute nested circles. The parameters of spiral lines can be adjusted to manipulate the tag capacity. We first define the number of spiral line layers and the cardinality as N and C, respectively. $C_{startpos}$ is the cardinality of starting position of the spiral line in term of angle in degrees for each layer, given the ability to rotate 360°, we set each possible starting position exactly 1° apart, resulting $C_{startpos} = 360$. C_{endpos} is the cardinality of ending position relative to starting position in degrees for any layer, this determines the length of the spiral line *length = endpos*.We set $C_{endpos} = 361$ to hold values 0 to 360, where 0 represents absence of spiral line and 360 represents a complete ring. In summary, the capacity contributed by spiral lines can be calculated as $(C_{startpos} \times (C_{endpos} - 2) + 2)^N$, where $(C_{endpos} - 2)$ acknowledges empty spiral line and full ring being same in any starting position.

Hollow: To allow a range of error tolerance, we develop hollow structure. As the ink takes time to sink into paper substrate, it can overlay with another line from the printer head, a hollow structure can reduce the probability that ink spreads and overlays on top of other undesired lines. In addition, enlarging hollow space can reduce ink usage and lower cost.

Connection: Adding connections increases tag capacity with the variations of connection between every two layers. We first define K, the number of connections between two layer, and C_K, the number of connections between adjacent layers. C_{KV} is the binary cardinality for each connection to be present or not, a connection is absent represented by KV = 0, and present presented with KV = 1. The capacity of connections alone can be calculated by ${C_{KV}}^{(C_K)^{(N-1)}}$.

Figure 11: Four different advanced ferrofluidic nested tag patterns.

Algorithm 1 Nested Pattern Design Generation in FerroTag

Input: N: The number of spiral line layer
R: Array of radius for spiral lines
L: Array of length of spiral lines
S: Array of starting point of spiral lines
K: Array of connection positions
Output: I: The generated tag pattern

```
Initialize N, R, L, S;
I.append(SpiralLine(index, 0, L, S));
index ← 1;
while index < N do                    ▷ Iterate for each component
    I.append(SpiralLine(index, R, L, S));
    I.append(Connection(index, R, R_{-1}, K));
    index + +;
end while
return I;
```

Tag Design: The design of ferrofluid nested pattern is illustrated in Algorithm 1. For a nested pattern (see Figure 11), the number of spiral line layers, radius of each spiral line, length of each spiral line, and starting position of each spiral line are preset by users

or randomly distributed as input. We establish *SpiralLine()* and *Connection()* functions based on the preset parameters. By calling these functions, array of tuples that stores spiral line and connection points are generated. The algorithm iterates layers by layers to generate tag patterns. In detail, the algorithm first transforms between polar coordinate and Cartesian coordinate, and then performs trigonometric calculations for each position such that pixel coordinates in the pattern are stored directly after calculation.

The Tag Capacity Estimation: We estimate the capacity of the tag with the model of Equation (5), where N is set as five for high capacity and proper size, and K is set as six to avoid overlapping connections as well as enable enough tag capacity. C_N is the total cardinality based on N. Based on these settings, the tag capacity can be mathematically modeled as follows:

$$\begin{cases} N > 1, C_K = 2, C_{KV} = 2, \\ C_{startpos} = 6, \\ C_{endpos} = 7, \\ C_N = (C_{startpos} \times (C_{endpos} - 2) + 2)^N \times {C_{KV}}^{(C_K)^{(N-1)}} \\ \quad = (6 \times (7-2))^5 \times (2^{2^4}) > 8.5 \times 10^{12}, \end{cases} \tag{5}$$

6 MMWAVE-SCANNABLE IDENTIFICATION SCHEME

6.1 *FerroRF* Response Signal Acquisition

We introduce the RF hardware in FerroTag to stimulate and acquire the *FerroRF* response from tags. Pulse-Doppler radar that emits a set of periodic powerful pulse signals has been largely used in airborne applications [46], such as the target range and shape detection. However, when a short-time pulse stimulus, which has an infinite frequency band, is applied to illuminate the electronics, the corresponding *FerroRF* response will be overlapped with the stimulus signal and difficult to recognize. Therefore, FerroTag selects a frequency-modulated continuous-wave (FMCW) radar with a narrow passband filter [60]. The FMCW radar continuously emits periodic narrow-band chirp signals whose frequency varies over time. Non-linear interrelation to these narrow-band stimuli will generate distinct frequency response, and the received signals will carry the distinguishable *FerroRF* responses when the stimuli signals hit the target tag. Specifically, the transmitted FMCW stimulation signal is formulated as Equation (6).

$$T(t) = e^{j(2\pi f_0 t + \int_0^t 2\pi\rho t \, dt)}, 0 < t < T_r, \tag{6}$$

where $T(t)$ is the transmitted signal, T_r is one chirp cycle, f_0 is the carrier frequency and ρ is the chirp rate. In our application, when $T(t)$ passes through the tag, the ferrofluidic patterns on the tag act as a passive convolutional processor (see Figure 2), and generates non-linear distortions to $T(t)$. After the manipulated signal radiates from the tag, the *non-linear spectrum response* will be captured by the RF probe receiver antenna (Rx). Once the *FerroRF* response signals are received, FerroTag will first preprocess the signal and extract the effective feature vector from the *FerroRF* response. After that, an identification model is developed to identify the tag.

6.2 Signal Preprocessing

In practice, the received *FerroRF* response always contain the signal distortion. A natural countermeasure is to model a digital filter and compensate for the distortion accordingly. However, such a solution hardly handles cumulative errors over time that are unlikely to be accessible to end-users [53]. To address this issue, we employ the range resolution analysis solution [51]. The range resolution is $\Delta RES = \frac{c}{2B}$, where c is the light speed, and B is the bandwidth of one periodic chirp. This solution can automatically align the signal distortion based on different conditions. When the distortion displacement $< \Delta RES$, the signal has a minute frequency shift that is invisible on the *FerroRF response*. When the distortion displacement $> \Delta RES$, it will result in the misalignment issue of the *FerroRF response*. To align spectrum response $S(w)$, we utilize the envelope correlation function between the shifted spectrum and its corresponding reference spectrum $Q_(w)$, formulated as:

$$E(\tau) = \sum_w |Q(w)| \cdot |S(w - \tau)|, \tag{7}$$

where τ is the frequency shift. The optimal frequency shift can be calculated as:

$$\tau^{opt} = \arg\max E(\tau). \tag{8}$$

Table 1: List of features extracted from the *FerroRF* response.

Category	Features
Temporal Feature	Mean Value, 50th percentile, 75th percentile, Standard Deviation, Skewness [49], Kurtosis [22], RMS Amplitude , Lowest Value, Highest Value
Spectral Feature	Mean Value, Standard Deviation, Skewness, Kurtosis, Crest Factor [11], Flatness [39]
Others	*MFCC-10* [64]

6.3 Spatial-temporal FerroTag Intrinsic Fingerprint Extraction

As the above mentioned, the *FerroRF* response contains the unique identity of the tag. As a result, we exploit the internal traits in the *FerroRF* response signal by extracting scalar features in spatial-temporal domains. The feature are listed in Table 1. These features represent the *FerroRF* response signal from different aspects. Notably, we employ 10 features in Mel-Frequency Cepstral Coefficients (MFCC) [64]. MFCC are coefficients, which are based on a linear cosine transform of a log power spectrum on a nonlinear Mel scale of frequency as illustrated in Equation (9), (10), and (11) [67].

$$B_m[k] = \begin{cases} 0, k < f_{m-1} \; and \; k > f_{m+1}, \\ \dfrac{k - f_{m-1}}{f_m - f_{m-1}}, f_{m-1} \le k \le f_m, \\ \dfrac{f_{m+1} - k}{f_{m+1} - f_m}, f_m \le k \le f_{m+1}, \end{cases} \tag{9}$$

$$Y[m] = \log(\sum_{k=f_{m-1}}^{f_{m+1}} |X[k]|^2 B_m[k]), \tag{10}$$

$$c[n] = \frac{1}{M} \sum_{m=1}^{M} Y[m] \cos(\frac{\pi n(m - 0.5)}{M}), \tag{11}$$

where $X[k]$ is the input signal applied by the Fast Fourier Transform (FFT), $B_m[k]$ is the Mel filter bank, $Y[m]$ is the Mel spectral coefficients, m is the number of filter bank, n is the number of cepstral coefficients. Intuitively, the fingerprint with more MFCC coefficients will contain more unique physical characteristics of the tag. MFCC combines the advantages of the cepstrum analysis with

a perceptual frequency scale based on critical bands, and can improve the tag recognition performance by boosting high-frequency energy and discovering more intrinsic information.

However, it also increases the computation overhead. To balance this trade-off, we empirically choose $n = 10$. Thus, MFCC-10 collectively make up the robust representation of the short-term power spectrum in the received signal, which is related to the tag pattern. Besides, apart from the MFCC-10, for example, the skewness is a scale of symmetry to judge if a distribution looks the same to the left and right of the center point, and flatness describes the degree to which they approximate the Euclidean space of the same dimensionality. Thus, after analyzing with the forward selection method for the feature selection [18], a fingerprint containing 25 features from the temporal and spectral parts is formed.

6.4 FerroTag Identification Algorithm

After we obtain the input data, a 25-dimensional feature vector extracted from the *FerroRF* response, we use FerroTag for the tag identification. We utilize our FerroTag identification algorithm which can be formulated as a multi-class classification problem as shown in Algorithm 2. A traditional approach to address this problem is the Convolutional Neural Network (CNN) classification. Although some scholars adopted the CNN approach in their particular applications [84], the CNN is intractable requiring intricate network topology tuning, long training time and complex parameters selection. Moreover, CNN based solutions, which learn features automatically, are not always effective due to the local convergence problem. Thus, we employ a customized random forest method, which is an ensemble learning method for classification task that operates by constructing a multitude of decision trees at training time and outputting the class that is the mode of the classes of the individual trees [42]. The advantage of adopting the random forest is that it utilizes the unbiased estimate to achieve the generalization error, and subsequently has an outstanding performance in generalization. Moreover, the random forest can resist the overfitting, be implemented without massive deployment and has an excellent ability to be interpreted [25]. Therefore, we use an ensemble learning method for classification of the *FerroRF* response signal. Particularly, we deploy a random forest with 150 decision trees as a suitable classifier for our system. The set of features selected through Section 6.3 are used to construct a multitude of decision trees at training stage to identify the corresponding tags for every 20ms segment of the RF signal in the classification stage.

6.5 Multiple Tags Counting and Identification

To further facilitate inventory management, FerroTag can count and identify multiple tags at the same time. This ability helps FerroTag with scanning multiple items in the same box or shelf, which can magnificently improve the scanning efficiency. To count the multiple tags, the spectral signature based solution is widely adopted [33]. The solutions detect if there are several wavelengths much greater than their footprints, when the designed tags resonate at frequencies. However, the resonation only occurs when the ink on the tag is conductive, while the ferrofluidic ink is the opposite. Thus, owing to multiple Rx on the probe, we employ the Angle of Arrival (AoA) to count the tags. The distances from the tags to

Algorithm 2 FerroTag Identification Algorithm

Input: γ: The *FerroRF* response traces from a tag
Output: R: The identification result

```
ϑ ← 150                                   ▷ Set the tree number
δ ← 0                                     ▷ Initial the count
ϱ(i) = Preprocessing(γ(i));               ▷ Preprocesse signal
for i ∈ {1, ..., n} do                    ▷ Extract features
    ϵ1(i) = FeaturesTemp(ϱ(i));
    ϵ2(i) = FeaturesFreq(ϱ(i));
    ϵ3(i) = FeaturesMFCC(ϱ(i));
    ϵ(i) = [ϵ1(i), ϵ2(i), ϵ3(i)];
end for
for i ∈ {1, ..., n} do
    R(i) = RandomForest(ϵ(i), ϑ);         ▷ Classify traces
    δ + +;
end for
return R
```

different Rx (the distance of propagation) vary, which causes phase shifts among the received signal on multiple Rx. The AoA solution is to calculate these phase shifts to induce tag signal sources and count tags [66]. The phase shifts $\Delta\omega$ can be formulated by:

$$\Delta\omega = \frac{2\pi\Delta d \sin\theta}{\lambda}, \tag{12}$$

where Δd is the distances between two Rx and θ is the AoA. According to the above equation, we can get the AoA resolution $\Delta\theta$ as:

$$\begin{aligned} \Delta\omega_{RES} = \frac{2\pi\Delta d_{\max}}{\lambda}(\sin(\theta+\Delta\theta) - \sin\theta) > \frac{2\pi}{\nu} \\ \xrightarrow{sin(\theta+\Delta\theta)-\sin\theta \approx \Delta\theta\cos\theta} \Delta\theta > \frac{\lambda}{\nu\Delta d_{\max}\cos\theta}, \end{aligned} \tag{13}$$

where ν is the number of sample points.

7 SYSTEM PROTOTYPE AND EVALUATION SETUP

Experimental Preparation: The deployment of FerroTag is shown in Figure 12. The distance between the tag and the probe is denoted as D. Note that D is adjustable based on the requirement of real applications. In this setting, D is set as 60cm empirically. The corresponding tag sizes are made in 28mm ($1.11in$) (diagonal). Each tag is attached to three standard boxes for scanning: two USPS package boxes and an Amazon package box.

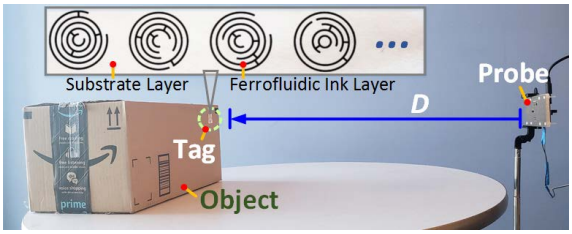

Figure 12: System implementation (designated FerroTags with a mmWave sensing probe).

FerroTag Fabrication: Without loss of the generality, we employ two off-the-shelf economic printers (i.e., Epson Expression Home

XP-400 and Canon Pixma MG2922) and retrofit printers to produce massive tags with 201 different nested patterns in the experiment. Each tag pattern is printed with different size (see Section 8.4 in detail). We collect a total of 300 traces with a 44.1K sampling rate for each tag, including 210 traces randomly selected for training and 90 traces for testing. As a result, there are entirely 42,210 traces for training and 18,090 for testing.

Application Protocol: FerroTag has the enrollment and identification mode. At the enrollment mode, FerroTag extracts features from tags introduced and stores them in a database. At the identification mode, FerroTag extracts features introduced and compares them to the template ones. FerroTag returns the tag ID and counts the object number.

Scanner Design: The FerroTag prototype employs an ordinal FMCW mmWave system [59]. The mmWave signal is processed using standard FMCW and antenna array equations to generate the *FerroRF* response, which is then utilized for the tag identification and counting. The transmission power is less than 1.2W. The cost is lower than $100. Besides, the probe can be easily mounted on the wall or integrated with other devices like laptops, smartphones, and mobile inspection instruments.

Performance Metric: To better evaluate the system performance, we adopted a confusion matrix, in addition to straightforward techniques such as accuracy, precision, and recall. In the confusion matrix plot, the darker the shade, the higher the classification performance [24].

8 FERROTAG SYSTEM EVALUATION

8.1 Identification Performance

We evaluate the ability of FerroTag to recognize the different tags in the controlled lab environment. The resulting average classification performance for each tag is shown on a heat map (aka. a confusion matrix) in Figure 14. The rows represent the selected tag ID classified by the random forest classifier and the columns represent the actual tag ID. Evidently, the diagonal cells are the darkest blue, implying that the traces from tag i were indeed classified as class i. While little light blue cells are appearing outside the diagonal cells, instances of misclassification are rare. The identification accuracy is 99.54%, with 99.52% precision and 99.49% recall, which implies that the feature vector effectively reflects the unique *FerroRF* response characteristics in each tag. To better illustrate the classification performance, we select ten types and enlarge their confusion matrices. Upon careful analysis, we notice that No.77 tag is misclassified as No.80 tag even though their shapes are significantly different. The reason is due to the nature of our algorithm which describes the *FerroRF* response, primarily based on the *FerroRF* effects, rather than their visual characteristics. In conclusion, our results demonstrate that paper-based printed tags can be precisely recognized by FerroTag.

8.2 FerroTag Sensing Tests

It is essential to detect and recognize tag identifies in a tagging infrastructure. To evaluate this performance, we employ the radar cross-section (RCS), that is an important characteristic that indicates the power of the backward tag signal [56]. The RCS can be

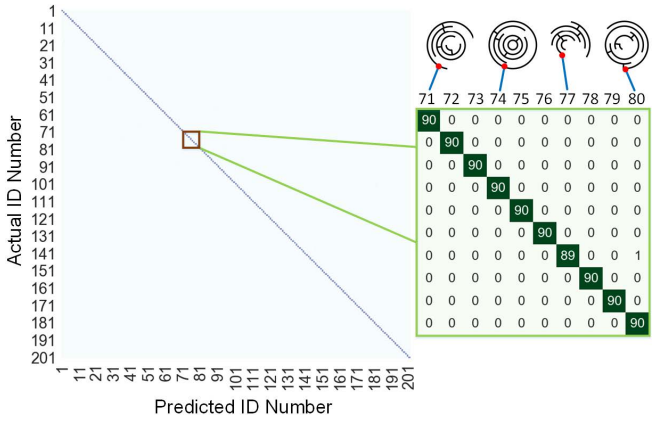

Figure 13: The identification performance for FerroTag with 201 different type tags. Confusion matrices of ten types are enlarged in the green box. These ten types are the same as others following the same pattern design. These ten types verify that most are classified correctly.

represented as:

$$\xi = \frac{P_r}{P_t G_t G_r} \frac{(4\pi)^3 d^4}{\lambda^2}, \tag{14}$$

where ξ is the RCS, P_r is the power of the received modulated tag signal, P_t is the power transmitted by the probe, G_t is the gain of the probe transmit antenna, G_r is the gain of the probe receive antenna, λ is the wavelength and d is the distance to the tag [20]. To evaluate the RCS of tags, we utilize 30 different tags. The RCS of the tags are between $-37dBsm$ to $-29dBsm$ under mmWave, which implies that the tag owns a similar exceptional performance to passive RFID tags [76].

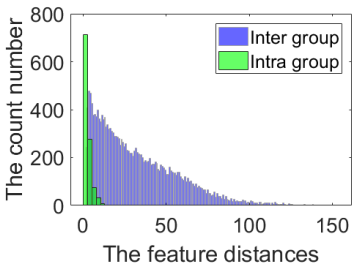

Figure 14: The tag uniqueness analysis

8.3 Tag Uniqueness

For a tagging infrastructure, it is essential to recognize the overall distinguishability of tags. In this evaluation, we employ 201 different fingerprints in Section 8.1 and differentiate the fingerprints into two groups, i.e., intra-group (within the same tag) and inter-group (among different tags). We leverage Euclidean distance, a widely used technique for measuring the fingerprint distance. The fingerprint distance between intra- and inter-groups is illustrated in Figure 14. The average of intra group is 2.51, which is significantly smaller than the average of inter group 32.04. Also the results show the tags can be completely separated with little overlap. Thereby, we prove the independence between two tags, even with the similar pattern.

8.4 Performance Characterization of Different FerroTag Configurations

In this section, to further reflect the actual performance in real practice (e.g., the tag size, the tag ink intensity, the reading rate, the tag pattern complexity and substrate material), we conduct the following experiments.

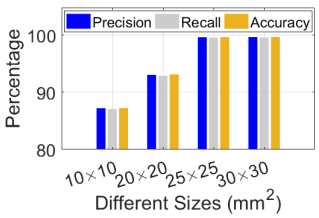

Figure 15: Tag detection and recognition with different sizes.

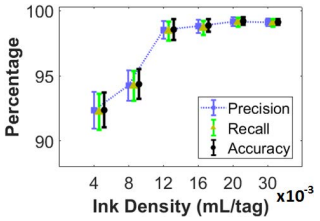

Figure 16: Performance under different ink densities.

Tag Size: The tag size is a crucial consideration in a real application, which is related to the tag cost and the occupancy. specifically, we design 50 different advanced tags with four different size settings between $10mm \times 10mm$ ($0.39in \times 0.39in$) to $30mm \times 30mm$ ($1.18in \times 1.18in$). For each size setting, we follow the same methodology described in Section 7 and re-prepare the training and testing set. Figure 15 shows the performance results. For the smallest size of $10mm \times 10mm$, FerroTag only obtains the accuracy of 87.22%. The results are because the ferrofluidic patterns are too small to be differentiated by the mmWave signal. After increasing the size, the performance gradually increases. Generally, we find that a turning point at $20mm \times 20mm$ where the performance saturates afterward (reaching the accuracy of 99.54%). Considering the printed-based tag, e.g., barcode, whose width is at least 30mm [10], the results imply that FerroTag is applicable for various applications.

Tag Ink Density: Intuitively, it is well known that the ink density of tags profoundly affects the tag cost. Thus, we propose to measure the tag ink intensity (mL/tag) that shows the ink amount usage for making a tag. We design 50 different advanced tags with six different density settings varying from $0.004mL/tag$ to $0.030mL/tag$ and evaluate how it affects the accuracy of the tag identification. Figure 16 shows the accuracy is only 92.7%. For the lowest ink density of $0.004mL/tag$, FerroTag only obtains 92.74% precision,92.62% recall and 92.76% accuracy, which shows that lower ink density can diminish the accuracy. The performance improves, along the ink density grows until $0.020mL/tag$. Then the performance keeps constant around 99.57% precision,99.52% recall and 99.59% accuracy. This observation can guide us to select the proper density to ensure the identification accuracy with a minimal cost in specific applications.

Scanning Time: We know that objects screening tasks are challenging due to concise budgeted time for efficiency. As a result, we are interested in analyzing the performance of FerroTag concerning different time budgets, *i.e.*, a different time needed for scanning one tag. Specifically, we select four different time settings between $5ms$ to $200ms$. For each time setting, we follow the same methodology described in Section 7 and re-prepare the training and testing set. Figure 17 shows the performance results. For the lowest duration of $5ms$, FerroTag only obtains the accuracy of 90.17%. The results

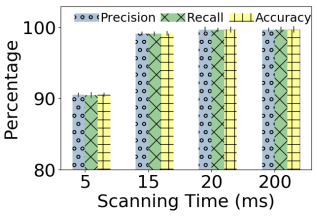

Figure 17: Tag identification with different scanning time.

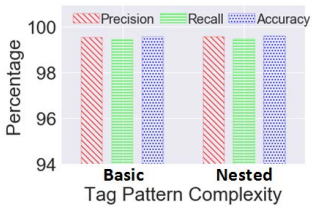

Figure 18: Performance under different tag complexities.

are because the contained information in traces with $5ms$ cannot comprehensively represent the characteristics of FerroTag. After increasing the scanning time, the performance gradually increases. Generally, we find that a turning point at $20ms$ where the performance saturates afterward (reaching 99.54% accuracy), which means we can scan 50 tags per second, which is a magnificent improvement in scanning speed compared to the optical-based solutions.

Tag Pattern Complexity: In the practical implementation, the tag pattern can be highly customized to satisfy different manufacture methods and appearance requirements. To understand its impact on the identification accuracy, we set *basic* group and *advanced* group according to the tag complexity and 50 different tags are employed for each. The results are shown in Figure 18. The identification accuracy for both groups remains high (above 99.1%), which implies that the system performance is insensitive to the tag pattern complexity.

Substrate Material: We consider the scenario where the user may use different substrates to build the tags according to various applications. Particularly, we collect four different daily-achievable materials as shown in Figure 19. The cumulative distribution function is plotted in the figure, where we can see that the overall identification error rate for each is less than 1%. Certain materials slightly affect the performance to some extent. This is because FerroTag utilizes high-frequency signal and therefore, has small wavelength and limited penetration ability. As a result, it is prone to the scattering reflection upon some specific materials. But in general, FerroTag still provides reliable performance in tag recognition.

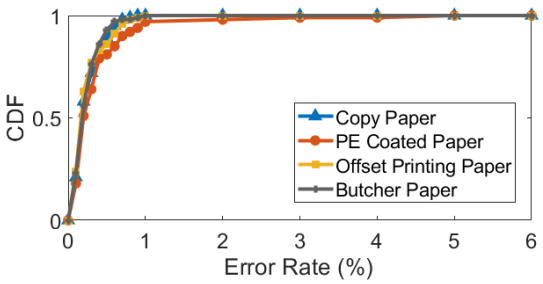

Figure 19: The objects detection under different substrate material.

9 ROBUSTNESS ANALYSIS

Performance in Different Distances: To validate the usability and effectiveness of FerroTag in the non-contact identification scenario, we set up the device to stimulate the operation distance from

30cm to 100cm considering the mmWave coverage of the tags in relation to their *response* magnitude. In this experiment, 50 different tags (see Section 7) are recruited. Figure 20 manifests that their performances can achieve up to 99.59% accuracy. Besides, the identification performance remains above 99% when the sensing distance varies within 1m. Thereby, FerroTag can facilitate in-situ and convenient tag scanning in real practice.

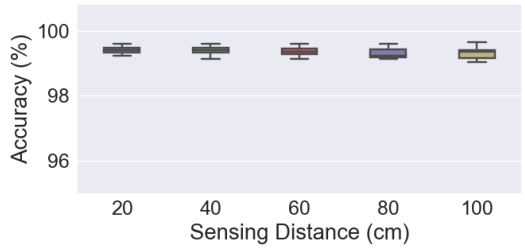

Figure 20: Performance under different sensing distances.

Impact of Environmental Dynamics: The ambient environment can introduce random noises or even interfere with the tag properties or the probe hardware operation. We consider common noises in the daily workplace in terms of human factors and ambient factors. Typically, we select four conditions where (1) the environment temperature is $10°C$ ($50°F$); (2) the humidity of the testing location is controlled at 70%; (3) the magnetic field strength is set at $400\mu T$; (4) the light intensity is $1000Lux$. Moreover, we use the result of the optimal lab environment as the comparison target (the temperature, the humidity, the magnetic field strength, the ultrasound wave and the light intensity are $20°C$ ($68°F$), 30%, $50\mu T$ and $300Lux$, respectively). Again, we evaluate the above four conditions using 50 tags. Figure 21 demonstrates that their performances all achieve above 99.14%. In conclusion, FerroTag presents a strong tolerance to different ambient environments.

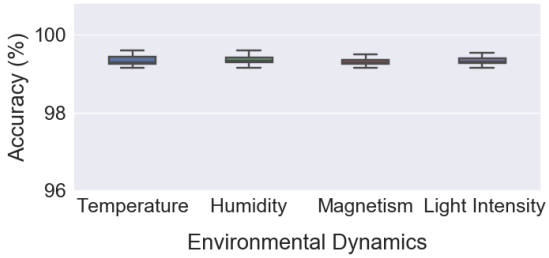

Figure 21: The tags detection under different environments.

Under Blockage: FerroTag usage scenarios may involve non-line of sight (NLOS) environment, e.g., in inventory management, where the object (and tag) may be placed inside a package. We mimic such NLOS cases by blocking the light of sight between the tag and probe using different materials: paper, wood, glass and plastic. Specifically, we evaluate the above four conditions using 50 tags. Figure 22 reveals that blockage has trivial impact on FerroTag's counting and identification. The experiment verifies that FerroTag works in NLOS scenarios where camera-based approaches will fail.

Impact of Scanning Orientation: In practical scenarios, tags may place towards different orientations. Therefore, it is important to investigate whether the sensing angle will affect system performance.

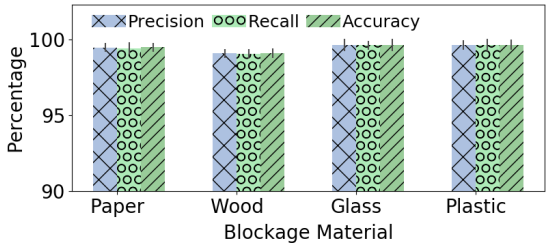

Figure 22: The tags detection under different occlusions.

Specifically, we measure the different tag orientations (from 0° to 180°). The results are shown in Figure 23. As for the orientation, the effective sensing range is among (60°-120°), since the mmWave has a narrow beam forming. Although the reflected signal slightly changes due to the different probe angles for each tag, the inter-device distinguishability among 30 tags is significant such that each tag can be correctly recognized. Thereby, FerroTag shows a strong capacity in real practice.

Durability Study: Proving the permanence of identification is crucial. Our generated dataset has included multiple sessions as part of a longitudinal approach to establishing a baseline comparison of long-term persistence. 30 different tags participated in the longitudinal study lasting three weeks as shown in Figure 24. Notably, this study has two phases: the enrollment phase and authentication phase. In the enrollment phase, training data were collected for each subject on the first day of this longitudinal study. Each tag finishes five trials in data collection events with the duration of each test set as 10 seconds. After that, the long-term authentication phase is carried out in the following three weeks. Each tag performed five identification trials every 2 days and each identification duration is 5 seconds in this study. The accuracy measurement is depicted in Fig 24. In the three weeks duration, mean values of accuracy measurement are between 99% and 100%, and standard deviations are between 0.22 and 0.51. We concluded that the accuracy has no significant performance decreasing or ascending tendency, which demonstrates FerroTag is robust against aging in time.

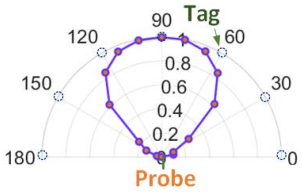

Figure 23: Impact of varying sensing angles.

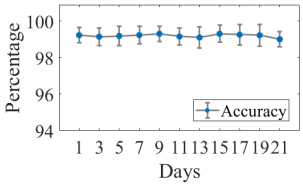

Figure 24: A three-week investigation on the accuracy stability of FerroTag.

10 A CASE STUDY ON COMPLEX SCENES

As the application environments of tags are mainly in retail, warehouse or places where a large amount of coexisting tags hidden in the package under NLOS environment, we aim to count their number and know their types immediately and conveniently without opening the package and protecting the privacy. To achieve this goal, there are two existing primary concerns in practice: 1) the unavoidable variance in the signal's scaling and magnitude; and 2) the interference from the containing items and the ambient

noises. To explore whether FerroTag can identify multiple hidden tags simultaneously, we continue with the setup in Section 7. Specifically, we employ 6 tags and select four conditions where: (i) and (iii) randomly select 2 tags, out of 6; (ii) and (iv) randomly select 3 tags, out of 6. In (i) and (ii), tags are attached to cardboard boxes within the package box, while in (iii) and (iv), tags are attached to T-shirts. This study is a 6-by-6 scanning with different combined. We enumerate all possible combinations in these conditions. Figure 25 shows the AoA range profile where the red color areas imply tag locations, and then we count the tags based on this range profile. The identification results are illustrated in Figure 26, showing that their performances keep between 97% to 99%. This is owing to the fact that the *FerroRF* effects change if we combine two tags along with the *FerroRF* response. To sum up, FerroTag suffices as an accurate and reliable way of ultra-low cost and in-situ tagging infrastructure in the real-world scene.

Figure 25: The graph shows the three tags counting.

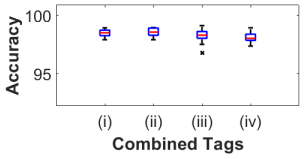

Figure 26: Identification of combined tags.

11 DISCUSSION

Potential Health Hazard: There are two aspects for the potential health consideration: wireless sensing and ferrofluidic prints. Compared to other wireless sensing techniques (e.g., WiFi spots), FerroTag has a much smaller radiation factor, e.g., a 1.2W power consumption and an 8dBm radio transmission power. Besides, the ferrofluidic ink is not inherently dangerous or toxic and has been applied to the medical domain [17]. Moreover, the ferrofluidic print can be naturally degradable [35, 61]. Therefore, FerroTag is a considerably safe identification tool with limited health hazard concerns.
Security and Privacy: Privacy-preserving is another fundamental factor for the object counting and identification as many owners have extremely high requirements on their privacy protection. Our system only requires the *FerroRF* response with a small information disclosure (i.e., mmWave signal) of the corresponding tag.
Custom Designed Patterns: It is significant to customize the dimensions of patterns as well as the paper substrate in FerroTag, to satisfy different application requirements. The system robustness to the tag size and pattern is discussed in Section 8.4.
Future Applications: Beyond the use case of the mass objects counting and identification, owing to the concept of the *FerroRF* effects and the advantages of ultra-low cost and in-situ, FerroTag can serve as a generic solution to extend the interaction area of IoT devices, extend the network to new physical dimensions, or serve as the 'fingertips' of the next-generation Internet. It can also be applied to a variety of applications, *e.g.*, agricultural monitoring, cell tracking, monitoring patients, and anti-counterfeiting [29, 50, 63, 68].

12 RELATED WORK

Paper-based (Chipless) Electronics: Paper-based electronics have been developed over the last few years. There are three categories in terms of the way to interact. The first one is the contact-based solution, that (e.g. microfluidic paper [70], wet sensor [38], touch sensor [27, 36], ubiquitous device [30, 31, 37, 54, 71], etc. However, they all need to measure the resistor, inductor, and capacitor (RLC) change in a contact manner, which are not convenient. The second category is based on a non-contact optical method. There are some research works, like linear barcode [7] and QR code [72]. However, these solutions are limited by the line of sight requirement. The solutions in the third category can work in a remote and invisible way, such as using the passive RFID [26, 32], ink-tattoo ID [29, 32] and mental-shape ID [23]. However, these solutions all employ the conductive ink or the complex toxic specific-designed chemical ink, which is neither low-cost nor environment-friendly. Up to date, no existing work utilizes the *FerroRF* effects to perform an ultra-low cost and naturally degradable tagging infrastructure.
mmWave Sensing: In recent years, mmWave has been utilized for the material characterization and object detection. There are two main mmWave sensing schemes. In the first category, these technologies are based on the detection of objects' geometry and micro-motion [34, 43–45, 52, 80, 86]. These mmWave sensing works mainly rely on analyzing the object boundaries and the Doppler effect of moving objects; thus their techniques cannot be applied to sense the intrinsic tag pattern. Second, there are some applications focusing on the material response for material component characterization [57, 58] and the non-linear response introduced by conductive components [40, 41] when stimulated by the mmWave signal. FerroTag is the first mmWave sensing work to combine the material response and the pattern design for identification.

13 CONCLUSION

In this paper, we presented a paper-based and mmWave-scannable tagging infrastructure FerroTag, to promote the inventory management technologies. FerroTag is easy to use and low-cost, which is on the basis of ferrofluidic ink on the paper print and its interference to the mmWave signal. In this study, we modeled the *FerroRF* effects to optimize the tag pattern design, prototyped an end-to-end FerroTag solution with a retrofited paper printer and a low-cost mmWave probe. Also, we developed a software framework of detecting and recognizing a newly designed nested tag pattern in practice. Extensive experiments, including one case study with complex scenes, imply that FerroTag can achieve the accuracy of 99.54% in a 20*ms* response time. Different levels of evaluation proved the effectiveness, reliability, and robustness of FerroTag. FerroTag has a potential to transform the sensing to new physical dimensions, and serve as the object identity of the next-generation Internet.

ACKNOWLEDGMENTS

We thank all anonymous reviewers for their insightful comments on this paper. This work was in part supported by the National Science Foundation under grant No. 1718375.

REFERENCES

[1] [n. d.]. 4 Types of Inventory Control Systems. ([n. d.]). https://www2.camcode.com/asset-tags/inventory-control-systems-types/

[2] [n. d.]. Inventory Management. ([n. d.]). https://searcherp.techtarget.com/definition/inventory-management

[3] [n. d.]. RFID vs Barcode: Comparison, Advantages & Disadvantages. ([n. d.]). https://www.peak-ryzex.com/articles/rfid-vs-barcode-comparison-advantages-disadvantages

[4] 2013. Policy: Sustainable development goals for people and planet. Nature 495, 7441 (2013), 305 – 307. http://search.ebscohost.com.gate.lib.buffalo.edu/login.aspx?direct=true&db=mnh&AN=EPTOC86214517&site=ehost-live&scope=site

[5] 2017. The Burgess Urban Land Use Model. (Dec 2017). https://transportgeography.org/?page_id=4908

[6] 2018. Printing Cost Calculator - Calculate Your Cost of Printing. (Jul 2018). https://www.uniprint.net/en/printing-cost-calculator-calculate-cost/

[7] Accessed: 2019-1-13. GS1 BARCODE CHART. http://www.gs1us.org/resources/standards/ean-upc-visuals.

[8] Accessed: 2019-1-3. MakingCosmetics - Triethanolamine - 2.0floz / 60ml - Cosmetic Ingredient. https://www.amazon.com/MakingCosmetics-Triethanolamine-2-0floz-60ml/dp/B01GDZYRK4/ref=sr_1_fkmrnull_1?

[9] Accessed: 2019-1-9. Staples Copy Paper Multi-Purpose Copier and Fax Machine Carton, Letter Size, Acid Free, 92 Bright, 20 lb, White, 5000 Sheets/Case. https://www.amazon.com/Staples-Multi-Purpose-Copier-Machine-Carton/dp/B00FGIFL0A/ref=sr_1_3?

[10] Accessed: 2019-2-15. Barcode Dimensions. https://worldbarcodes.com/barcode-standards/.

[11] Accessed: 2019-2-16. Crest factor. https://en.wikipedia.org/wiki/Crest_factor.

[12] Accessed: 2019-2-3. Epson Expression Home XP-440 Wireless Color Photo Printer with Scanner and Copier, Amazon Dash Replenishment Enabled. https://www.amazon.com/gp/product/B06W9K5FD2/ref=oh_aui_search_asin_title?ie=UTF8&psc=1.

[13] Accessed: 2019-4-5. 10 Shocking Inventory Management Statistics. https://blog.capterra.com/inventory-management-statistics/.

[14] Accessed: 2019-4-5. Everything You Need to Know About Inventory Management. https://www.warehouseanywhere.com/resources/inventory-management/.

[15] Accessed: 2019-4-5. Which area are you investing in most heavily to evolve your inventory management practices? https://www.statista.com/statistics/780763/inventory-management-investments-retailers-manufacturers/.

[16] Accessed: 2019-8-10. YARONGTECH UHF tag. https://www.amazon.com/YARONGTECH-860-960MHZ-Alien-73-5x21-2mm-Adhesive/dp/B01L97ULR4/[2].

[17] Christoph Alexiou, Roland Jurgons, Roswitha J Schmid, Christian Bergemann, Julia Henke, Wolf Erhard, Ernst Huenges, and Fritz Parak. 2003. Magnetic drug targeting - biodistribution of the magnetic carrier and the chemotherapeutic agent mitoxantrone after locoregional cancer treatment. Journal of drug targeting 11, 3 (2003), 139–149.

[18] F Guillaume Blanchet, Pierre Legendre, and Daniel Borcard. 2008. Forward selection of explanatory variables. Ecology 89, 9 (2008), 2623–2632.

[19] Christian Carlowitz, Axel Strobel, Tobias Schäfer, Frank Ellinger, and Martin Vossiek. 2012. A mm-wave RFID system with locatable active backscatter tag. In 2012 IEEE International Conference on Wireless Information Technology and Systems (ICWITS). IEEE, 1–4.

[20] Luca Catarinucci, Danilo De Donno, Matteo Guadalupi, Fabio Ricciato, and Luciano Tarricone. 2011. Performance analysis of passive UHF RFID tags with GNU-radio. In 2011 IEEE International Symposium on Antennas and Propagation (APSURSI). IEEE, 541–544.

[21] Shilin Chen, Hui Yao, Jianping Han, Chang Liu, Jingyuan Song, Linchun Shi, Yingjie Zhu, Xinye Ma, Ting Gao, Xiaohui Pang, et al. 2010. Validation of the ITS2 region as a novel DNA barcode for identifying medicinal plant species. PloS one 5, 1 (2010), e8613.

[22] Robert I Davis, Wei Qiu, Nicholas J Heyer, Yiming Zhao, MS Qiuling Yang, Nan Li, Liyuan Tao, Liangliang Zhu, Lin Zeng, Daohua Yao, et al. 2012. The use of the kurtosis metric in the evaluation of occupational hearing loss in workers in China: Implications for hearing risk assessment. Noise and Health 14, 61 (2012), 330.

[23] Gerald DeJean, Vasileios Lakafosis, Anya Traille, Hoseon Lee, Edward Gebara, Manos Tentzeris, and Darko Kirovski. 2011. RFDNA: A wireless authentication system on flexible substrates. In 2011 IEEE 61st Electronic Components and Technology Conference (ECTC). IEEE, 1332–1337.

[24] Sanorita Dey, Nirupam Roy, Wenyuan Xu, Romit Roy Choudhury, and Srihari Nelakuditi. 2014. AccelPrint: Imperfections of Accelerometers Make Smartphones Trackable.. In NDSS.

[25] Jerome Friedman, Trevor Hastie, and Robert Tibshirani. 2001. The elements of statistical learning. Vol. 1. Springer series in statistics New York.

[26] Chuhan Gao, Yilong Li, and Xinyu Zhang. 2018. LiveTag: Sensing human-object interaction through passive chipless WiFi tags. In 15th {USENIX} Symposium on Networked Systems Design and Implementation ({NSDI} 18). 533–546.

[27] Chuhan Gao, Xinyu Zhang, and Suman Banerjee. 2018. Conductive Inkjet Printed Passive 2D TrackPad for VR Interaction. In Proceedings of the 24th Annual International Conference on Mobile Computing and Networking. ACM, 83–98.

[28] Jerry Zeyu Gao, Lekshmi Prakash, and Rajini Jagatesan. 2007. Understanding 2d-barcode technology and applications in m-commerce-design and implementation of a 2d barcode processing solution. In 31st Annual International Computer Software and Applications Conference (COMPSAC 2007), Vol. 2. IEEE, 49–56.

[29] Moshe Glickstein. 2004. Firewall protection for paper documents. RFID Journal internet article, Feb (2004).

[30] Nan-Wei Gong, Steve Hodges, and Joseph A Paradiso. 2011. Leveraging conductive inkjet technology to build a scalable and versatile surface for ubiquitous sensing. In Proceedings of the 13th international conference on Ubiquitous computing. ACM, 45–54.

[31] Nan-Wei Gong, Steve Hodges, and Joseph A. Paradiso. 2011. Leveraging Conductive Inkjet Technology to Build a Scalable and Versatile Surface for Ubiquitous Sensing. In Proceedings of the 13th International Conference on Ubiquitous Computing (UbiComp '11). ACM, New York, NY, USA, 45–54. https://doi.org/10.1145/2030112.2030120

[32] Takahiro Hashizume, Takuya Sasatani, Koya Narumi, Yoshiaki Narusue, Yoshihiro Kawahara, and Tohru Asami. 2016. Passive and contactless epidermal pressure sensor printed with silver nano-particle ink. In Proceedings of the 2016 ACM International Joint Conference on Pervasive and Ubiquitous Computing. ACM, 190–195.

[33] Cristian Herrojo, Jordi Naqui, Ferran Paredes, and Ferran Martín. 2016. Spectral signature barcodes implemented by multi-state multi-resonator circuits for chipless RFID tags. In 2016 IEEE MTT-S International Microwave Symposium (IMS). IEEE, 1–4.

[34] M. C. Huang, J. J. Liu, W. Xu, C. Gu, C. Li, and M. Sarrafzadeh. 2016. A Self-Calibrating Radar Sensor System for Measuring Vital Signs. IEEE Transactions on Biomedical Circuits and Systems 10, 2 (April 2016), 352–363.

[35] Robert Kaiser. 1972. Ferrofluid composition. (Oct. 24 1972). US Patent 3,700,595.

[36] Çağdaş Karataş and Marco Gruteser. 2015. Printing multi-key touch interfaces. In Proceedings of the 2015 ACM International Joint Conference on Pervasive and Ubiquitous Computing. ACM, 169–179.

[37] Yoshihiro Kawahara, Steve Hodges, Benjamin S Cook, Cheng Zhang, and Gregory D Abowd. 2013. Instant inkjet circuits: lab-based inkjet printing to support rapid prototyping of UbiComp devices. In Proceedings of the 2013 ACM international joint conference on Pervasive and ubiquitous computing. ACM, 363–372.

[38] Yoshihiro Kawahara, Hoseon Lee, and Manos M Tentzeris. 2012. Sensprout: Inkjet-printed soil moisture and leaf wetness sensor. In Proceedings of the 2012 ACM Conference on Ubiquitous Computing. ACM, 545–545.

[39] Benjamin L'Huillier and Arman Shafieloo. 2017. Model-independent test of the FLRW metric, the flatness of the Universe, and non-local estimation of H0 rd. Journal of Cosmology and Astroparticle Physics 2017, 01 (2017), 015.

[40] Zhengxiong Li, Fenglong Ma, Aditya Singh Rathore, Zhuolin Yang, Baicheng Chen, Lu Su, and Wenyao Xu. 2020. WaveSpy: Remote and Through-wall Screen Attack via mmWave Sensing. In To appear in IEEE Symposium on Security and Privacy 2020 (S&P'20).

[41] Zhengxiong Li, Zhuolin Yang, Chen Song, Changzhi Li, Zhengyu Peng, and Wenyao Xu. 2018. E-Eye: Hidden Electronics Recognition through mmWave Nonlinear Effects. In Proceedings of the 16th ACM Conference on Embedded Networked Sensor Systems. ACM, 68–81.

[42] Andy Liaw, Matthew Wiener, et al. 2002. Classification and regression by randomForest. R news 2, 3 (2002), 18–22.

[43] Jaime Lien, Nicholas Gillian, M. Emre Karagozler, Patrick Amihood, Carsten Schwesig, Erik Olson, Hakim Raja, and Ivan Poupyrev. 2016. Soli: Ubiquitous Gesture Sensing with Millimeter Wave Radar. ACM Trans. Graph. 35, 4, Article 142 (July 2016), 19 pages. https://doi.org/10.1145/2897824.2925953

[44] Feng Lin, Chen Song, Yan Zhuang, Wenyao Xu, Changzhi Li, and Kui Ren. 2017. Cardiac Scan: A Non-contact and Continuous Heart-based User Authentication System. In Proceedings of the 23rd Annual International Conference on Mobile Computing and Networking (MobiCom '17). ACM, New York, NY, USA, 315–328.

[45] F. Lin, Y. Zhuang, C. Song, A. Wang, Y. Li, C. Gu, C. Li, and W. Xu. 2017. SleepSense: A Noncontact and Cost-Effective Sleep Monitoring System. IEEE Transactions on Biomedical Circuits and Systems 11, 1 (Feb 2017), 189–202.

[46] Bassem R Mahafza. 2017. Introduction to radar analysis. Chapman and Hall/CRC.

[47] Heikki Mannila and Pekka Orponen. 2010. Algorithms and Applications. Springer.

[48] Wenguang Mao, Mei Wang, and Lili Qiu. 2018. AIM: Acoustic Imaging on a Mobile. In Proceedings of the 16th Annual International Conference on Mobile Systems, Applications, and Services (MobiSys '18). ACM, New York, NY, USA, 468–481. https://doi.org/10.1145/3210240.3210325

[49] Kanti V Mardia. 1970. Measures of multivariate skewness and kurtosis with applications. Biometrika 57, 3 (1970), 519–530.

[50] Moataz M Mekawy, Atsushi Saito, Akira Sumiyoshi, Jorge J Riera, Hiroaki Shimizu, Ryuta Kawashima, and Teiji Tominaga. 2019. Hybrid magneto-fluorescent nano-probe for live apoptotic cells monitoring at brain cerebral

ischemia. Materials Science and Engineering: C (2019).
[51] Adriano Meta, Peter Hoogeboom, and Leo P Ligthart. 2007. Signal processing for FMCW SAR. IEEE Transactions on Geoscience and Remote Sensing 45, 11 (2007), 3519–3532.
[52] I. V. Mikhelson, S. Bakhtiari, T. W. Elmer II, and A. V. Sahakian. 2011. Remote Sensing of Heart Rate and Patterns of Respiration on a Stationary Subject Using 94-GHz Millimeter-Wave Interferometry. IEEE Transactions on Biomedical Engineering 58, 6 (June 2011), 1671–1677. https://doi.org/10.1109/TBME.2011.2111371
[53] José M Muñoz-Ferreras and Félix Pérez-Martínez. 2010. Subinteger range-bin alignment method for ISAR imaging of noncooperative targets. EURASIP Journal on Advances in Signal Processing 2010 (2010), 14.
[54] Koya Narumi, Steve Hodges, and Yoshihiro Kawahara. 2015. ConductAR: an augmented reality based tool for iterative design of conductive ink circuits. In Proceedings of the 2015 ACM International Joint Conference on Pervasive and Ubiquitous Computing. ACM, 791–800.
[55] Pavel V Nikitin, Sander Lam, and KVS Rao. 2005. Low cost silver ink RFID tag antennas. In 2005 IEEE Antennas and Propagation Society International Symposium, Vol. 2. IEEE, 353–356.
[56] Pavel V Nikitin, KVS Rao, and Roberto D Martinez. 2007. Differential RCS of RFID tag. Electronics Letters 43, 8 (2007), 431–432.
[57] Turgut Ozturk. 2019. Characterization of Liquids Using Electrical Properties in Microwave and Millimeter Wave Frequency Bands. Journal of Nondestructive Evaluation 38, 1 (2019), 11.
[58] Turgut Ozturk. 2019. Classification of measured unsafe liquids using microwave spectroscopy system by multivariate data analysis techniques. Journal of hazardous materials 363 (2019), 309–315.
[59] Zhengyu Peng, José-María Muñoz-Ferreras, Roberto Gómez-García, Lixin Ran, and Changzhi Li. 2016. 24-GHz biomedical radar on flexible substrate for ISAR imaging. In Wireless Symposium (IWS), 2016 IEEE MTT-S International. IEEE, 1–4.
[60] Zhengyu Peng, Lixin Ran, and Changzhi Li. 2015. A 24-GHz low-cost continuous beam steering phased array for indoor smart radar. In 2015 IEEE 58th International Midwest Symposium on Circuits and Systems (MWSCAS). IEEE, 1–4.
[61] R Perez-Castillejos, J Esteve, MC Acero, and JA Plaza. 2001. Ferrofluids for disposable microfluidic systems. In Micro Total Analysis Systems 2001. Springer, 492–494.
[62] Jukka Perkiö and Aapo Hyvärinen. 2009. Modelling image complexity by independent component analysis, with application to content-based image retrieval. In International Conference on Artificial Neural Networks. Springer, 704–714.
[63] Stevan Preradovic, Isaac Balbin, and Nemai Karmakar. 2008. The development and design of a novel chipless RFID system for low-cost item tracking. In 2008 Asia-Pacific Microwave Conference. IEEE, 1–4.
[64] Zakariya Qawaqneh, Arafat Abu Mallouh, and Buket D Barkana. 2017. Deep neural network framework and transformed MFCCs for speaker's age and gender classification. Knowledge-Based Systems 115 (2017), 5–14.
[65] Jie Ren, Lin Wang, Yuefeng Mo, Chen Feng, Yunxin Ouyang, Hui Li, and Jun Yin. 2019. Illuminator for a barcode scanner. (Feb. 21 2019). US Patent App. 16/055,776.
[66] Peng Rong and Mihail L Sichitiu. 2006. Angle of arrival localization for wireless sensor networks. In 2006 3rd annual IEEE communications society on sensor and ad hoc communications and networks, Vol. 1. Ieee, 374–382.
[67] Md Sahidullah and Goutam Saha. 2012. Design, analysis and experimental evaluation of block based transformation in MFCC computation for speaker recognition. Speech Communication 54, 4 (2012), 543–565.
[68] Adeel Saleem, Atif Iqbal, Adnan Sabir, and Adil Hussain. 2019. Real-Time Physical Changing 3d Display using Magnetic Liquid Technology for Visually Impaired Patients. In 2019 2nd International Conference on Computing, Mathematics and Engineering Technologies (iCoMET). IEEE, 1–5.
[69] S. Scherr, S. Ayhan, B. Fischbach, A. Bhutani, M. Pauli, and T. Zwick. 2015. An Efficient Frequency and Phase Estimation Algorithm With CRB Performance for FMCW Radar Applications. IEEE Transactions on Instrumentation and Measurement 64, 7 (July 2015), 1868–1875. https://doi.org/10.1109/TIM.2014.2381354
[70] Hiroyuki Shibata, Yuki Hiruta, and Daniel Citterio. 2019. Fully inkjet-printed distance-based paper microfluidic devices for colorimetric calcium determination using ion-selective optodes. Analyst (2019).
[71] Tung Ta, Masaaki Fukumoto, Koya Narumi, Shigeki Shino, Yoshihiro Kawahara, and Tohru Asami. 2015. Interconnection and double layer for flexible electronic circuit with instant inkjet circuits. In Proceedings of the 2015 ACM International Joint Conference on Pervasive and Ubiquitous Computing. ACM, 181–190.
[72] Iuliia Tkachenko, William Puech, Christophe Destruel, Olivier Strauss, Jean-Marc Gaudin, and Christian Guichard. 2016. Two-level QR code for private message sharing and document authentication. IEEE Transactions on Information Forensics and Security 11, 3 (2016), 571–583.
[73] DA Usanov, AV Skripal, and SA Ermolaev. 1996. Microwave and Ultrasound Methods for Determining the Size of Ferromagnetic Particles and Magnetic Fluid Agglomerates. MAGNETOHYDRODYNAMICS C/C OF MAGNITNAIA GIDRODINAMIKA 32 (1996), 481–486.
[74] DA Usanov, Al V Skripal, An V Skripal, and AV Kurganov. 2001. Determination of the magnetic fluid parameters from the microwave radiation reflection coefficients. Technical Physics 46, 12 (2001), 1514–1517.
[75] Marco Vari and Dajana Cassioli. 2014. mmWaves RSSI indoor network localization. In 2014 IEEE International Conference on Communications Workshops (ICC). IEEE, 127–132.
[76] Arnaud Vena, Etienne Perret, Smail Tedjini, Guy Eymin Petot Tourtollet, Anastasia Delattre, Frédéric Garet, and Yann Boutant. 2013. Design of chipless RFID tags printed on paper by flexography. IEEE Transactions on Antennas and Propagation 61, 12 (2013), 5868–5877.
[77] W Voit, DK Kim, W Zapka, M Muhammed, and KV Rao. 2001. Magnetic behavior of coated superparamagnetic iron oxide nanoparticles in ferrofluids. MRS Online Proceedings Library Archive 676 (2001).
[78] Anran Wang, Vikram Iyer, Vamsi Talla, Joshua R Smith, and Shyamnath Gollakota. 2017. {FM} Backscatter: Enabling Connected Cities and Smart Fabrics. In 14th {USENIX} Symposium on Networked Systems Design and Implementation ({NSDI} 17). 243–258.
[79] Chen Wang, Jian Liu, Yingying Chen, Hongbo Liu, and Yan Wang. 2018. Towards In-baggage Suspicious Object Detection Using Commodity WiFi. 2018 IEEE Conference on Communications and Network Security (CNS) (2018), 1–9.
[80] Teng Wei and Xinyu Zhang. 2015. mtrack: High-precision passive tracking using millimeter wave radios. In Proceedings of the 21st Annual International Conference on Mobile Computing and Networking. ACM, 117–129.
[81] Teng Wei and Xinyu Zhang. 2016. Gyro in the air: tracking 3D orientation of batteryless internet-of-things. In Proceedings of the 22nd Annual International Conference on Mobile Computing and Networking. ACM, 55–68.
[82] Peter Welch. 1967. The use of fast Fourier transform for the estimation of power spectra: a method based on time averaging over short, modified periodograms. IEEE Transactions on audio and electroacoustics 15, 2 (1967), 70–73.
[83] Klaus Witrisal, Paul Meissner, Erik Leitinger, Yuan Shen, Carl Gustafson, Fredrik Tufvesson, Katsuyuki Haneda, Davide Dardari, Andreas F Molisch, Andrea Conti, et al. 2016. High-accuracy localization for assisted living: 5G systems will turn multipath channels from foe to friend. IEEE Signal Processing Magazine 33, 2 (2016), 59–70.
[84] Lauren J Wong, William C Headley, Seth Andrews, Ryan M Gerdes, and Alan J Michaels. 2018. Clustering Learned CNN Features from Raw I/Q Data for Emitter Identification. In MILCOM 2018-2018 IEEE Military Communications Conference (MILCOM). IEEE, 26–33.
[85] Mingmin Zhao, Yonglong Tian, Hang Zhao, Mohammad Abu Alsheikh, Tianhong Li, Rumen Hristov, Zachary Kabelac, Dina Katabi, and Antonio Torralba. 2018. RF-based 3D skeletons. In Proceedings of the 2018 Conference of the ACM Special Interest Group on Data Communication. ACM, 267–281.
[86] Yibo Zhu, Yanzi Zhu, Zengbin Zhang, Ben Y Zhao, and Haitao Zheng. 2015. 60GHz mobile imaging radar. In Proceedings of the 16th International Workshop on Mobile Computing Systems and Applications. ACM, 75–80.